

# Strain-ultrasensitive surface wrinkles for visual wearable optical sensor

**Tianjiao Ma**

Shanghai Jiao Tong University <https://orcid.org/0000-0002-1011-8753>

**Shuai Chen**

Shanghai Jiao Tong University

**Jin Li**

**Jie Yin**

Shanghai Jiao Tong University

**Xuesong Jiang** (✉ [ponygle@sjtu.edu.cn](mailto:ponygle@sjtu.edu.cn))

Shanghai Jiao Tong University <https://orcid.org/0000-0002-8976-8491>

---

## Article

**Keywords:** wearable sensor, optical sensor, surface wrinkles, strain, interactively visualize

**Posted Date:** February 28th, 2022

**DOI:** <https://doi.org/10.21203/rs.3.rs-1357096/v1>

**License:**   This work is licensed under a Creative Commons Attribution 4.0 International License.

[Read Full License](#)

---

# Strain-ultrasensitive surface wrinkles for visual wearable optical sensor

Tianjiao Ma, Shuai Chen, Jin Li, Jie Yin, Xuesong Jiang\*

School of Chemistry& Chemical Engineering, Frontiers Science Center for Transformative Molecules, State Key Laboratory for Metal Matrix Composite Materials, Shanghai Jiao Tong University, Shanghai 200240, P. R. China

\*Corresponding author. E-mail: ponygle@sjtu.edu.cn

**ABSTRACT:** Wearable tactile sensors have found widespread applications in human health monitoring, motion monitoring, human-machine interaction, and artificial prostheses. Herein, we demonstrate a new and feasible strategy for wearable optical sensors based on surface wrinkles ultrasensitive to strain using a bilayer wrinkling system, in which the sensing mechanism is different from that of the traditional electrical sensors. The strain ( $\vec{S}(\varepsilon, \theta_S)$ ), the wrinkled topography ( $\vec{W}(A, \theta_W)$ ), and the reflected optical signal ( $\vec{O}(\delta, \theta_O)$ ) functions are correlated with each other, allowing simultaneous measurement of strain magnitude and direction due to the vector property of optical signals. In addition, interactively visualized detection of slight strain has been achieved by conspicuous structural color change, successfully amplifying the strain signal owing to the ultra-sensitivity of wrinkles and the nonlinearity of optical signal. The sensor also exhibits electrical safety and immunity to electromagnetic interference, and thus may find potential applications in detecting various complex slight strains, such as subtle human motion or object deformation.

**Keywords:** wearable sensor, optical sensor, surface wrinkles, strain, interactively visualize

## Introduction

Wearable tactile sensors, especially strain and pressure sensors, can convert the mechanical property data of an object or human body into measurable signals<sup>1, 2</sup>, such as electrical signals (resistance or capacitance), optical signals, or magnetic signals. As an important component in electronic skin or flexible wearable devices, wearable tactile sensors have found widespread applications in human health monitoring<sup>3-6</sup>, motion monitoring<sup>5-8</sup>, human-machine interaction<sup>9-11</sup>, and artificial prosthesis<sup>12, 13</sup>. Currently, much effort has been made to develop strain or pressure sensors with high sensitivity and stretchability<sup>2, 14-16</sup>. Among them, resistive sensors detect the strain or pressure through changes in the intrinsic resistance<sup>17-20</sup>, contact resistance<sup>7, 20-22</sup>, or conductive filler networks in stretchable matrices<sup>18, 23-25</sup>. Capacitive sensors detect signals due to geometrical deformation<sup>17, 26, 27</sup> or changes in the effective dielectric constant<sup>17, 26</sup>. These types of sensors usually possess high sensitivity, stretchability, linearity, and durability. In addition, several optical or magnetic sensors have been fabricated utilizing waveguides<sup>28, 29</sup>, light-emitting diodes<sup>30-32</sup>, photonic crystals<sup>33, 34</sup>, and magnetic microparticles<sup>35</sup>.

Significant progress has been made towards enhancing the performance of sensors<sup>2, 14-16</sup>. However, most of the studies were limited to the basic sensing mechanism, which is commonly a traditional electrical mechanism. Thus, a different sensing method may provide a significant reference and overcome the limitations, inspiring people to broaden their research routes. Surface micro/nanoscale wrinkles often found in layered systems of soft materials<sup>36-39</sup> possess the ability to manipulate light propagation, such as reflection, scattering, and diffraction<sup>40-45</sup>. These may provide an alternative mechanism for optical strain sensors because of the dependence of the topography evolution of surface wrinkles and corresponding optical signals on the external strain. Compared with other strain sensors, a wrinkle-based optical sensor exhibits a series of unique advantages. Most strain sensors can only detect the strain degree but not the strain direction, which is necessary for the application of strain sensors in complex states<sup>46, 47</sup>. Some studies have enabled the sensors to measure strain direction by orthogonally stacking two sensors<sup>46, 48</sup>, which is accompanied by the

complexity of measuring and decoupling the signals. Wrinkle-based optical sensors can detect the strain direction and magnitude simultaneously by a single signal in one sensor, owing to the good use of the vector property of the optical signal. On the other hand, in commonly used electrical sensors, electrical signal processing and integrated human-readable readout devices are necessary because electrical signals cannot be directly visualized by human eyes. Compared with electrical signals, optical signals offer the advantage of the interactively visualized detection of strain by users through color change<sup>33, 34</sup> or brightness change<sup>31, 49, 50</sup>, thus simplifying the external instruments and broadening the sensor applications. Furthermore, if surface wrinkles are ultrasensitive to strain, the resulting optical signal possesses a nonlinear amplification effect on the wrinkled topography, which might provide an ultrasensitive sensor for strain. In addition, wrinkle-based optical sensors exhibit some advantages of electrical safety and immunity to electromagnetic interference. Although there are still a few issues to be addressed, wrinkle-based optical sensors are a promising approach for realization of wearable strain sensors.

Herein, we demonstrate a new and feasible strategy for the development of wearable optical sensors based on surface wrinkles ultrasensitive to strain (**Fig. 1**). Either random wrinkles or ordered wrinkles undergo topography evolution under an external strain. The resulting structures were found to rely on strain direction and magnitude. The reflected optical signal corresponding to the wrinkled structures illustrated the information of the external strain. By accurately measuring the optical signal, not only the strain degree could be obtained but also the strain direction without the complex decoupling process. On the other hand, surface wrinkles with strong light scattering increased the viewable angle and visibility of the film interference color, whereas the flat surface limited the appearance. Thus, it displayed an interactively visualized appearance change when the ordered wrinkles underwent axial strain and became flat. Furthermore, owing to the bottom-up method of the wrinkling process, these sensors based on wrinkles possess a higher sensitivity ( $\sim 1.5\%$ ) compared to other visualized optical strain sensors. Therefore, the proposed strategy provides an alternative for wearable optical sensors with convenient strain direction and magnitude

detection, interactively visualized measurement, and relatively high sensitivity, which may find potential applications in small strain detection such as human slight motion and vibration of objects.

## Results

### Strategy of wrinkles-based wearable optical sensor

The entire strategy for the fabrication of a wearable optical sensor based on surface wrinkles ultrasensitive to strain is illustrated in **Fig. 1**. A bilayer wrinkling system was utilized to form surface wrinkles, with poly(dimethylsiloxane) (PDMS) serving as the substrate and a spin-coated film of an anthracene-containing copolymer (PAN-BA) as the skin layer. A detailed preparation is shown in the **Methods**. The anthracene (AN) group enabled selective wrinkling owing to its sensitivity to ultraviolet (UV) light<sup>51</sup>. After photodimerization of the AN group, the polymer network was crosslinked, and the modulus of the top film increased. According to the linear buckling theory, random wrinkles are formed under thermal treatment and subsequent cooling to room temperature owing to the mismatch in the moduli and thermal expansion coefficients between the stiff skin layer and the soft substrate. Furthermore, if the irradiation process is performed with a striped photomask, ordered wrinkles are formed in the exposed area owing to the in-plane asymmetric distribution of stress<sup>45</sup>.

Either random wrinkles or ordered wrinkles undergo topography evolution under external strain. As shown in **Fig. 1a**, random wrinkles became ordered under stretching and returned to their initial state after releasing the applied strain. This was attributed to the mechanism whereby wrinkles parallel to the uniaxial strain direction gradually became flat with a decreasing amplitude ( $A$ ), while wrinkles perpendicular to the strain direction grew owing to the Poisson effect. As a result, random wrinkles gradually evolved, and finally converted into ordered wrinkles, in which the direction was perpendicular to the applied strain. Simultaneously, the corresponding reflected diffraction pattern of light evolved from concentric rings to ellipses and finally to a line, in agreement with the Fourier transform. Importantly, the orientation of the resulting diffraction pattern was parallel to the wrinkle direction and perpendicular to the strain

direction, and the lengths of the diffraction pattern in both directions were functionally correlated with the strain magnitude. In other words, both the magnitude ( $\varepsilon$ ) and direction ( $\theta_S$ ) of strain ( $\vec{S}(\varepsilon, \theta_S)$ ) are functions of the amplitude ( $A$ ) and direction ( $\theta_W$ ) of the wrinkle ( $\vec{W}(A, \theta_W)$ ), and further, the function correlates with the optical signals, such as the viewable angle ( $\delta$ ) and orientation ( $\theta_O$ ) of the viewable field ( $\vec{O}(\delta, \theta_O)$ ), which can be obtained from the diffraction patterns. Therefore, it provides an alternative method for detecting both the strain degree and direction using the reflected optical signal.

A schematic illustration of visualized strain detection is shown in **Fig. 1b**. Under uniaxial strain parallel to the wrinkle direction, the ordered wrinkles gradually became flat. In the initial state, surface wrinkles caused strong light scattering, which plays an important role in humans seeing the objects from all directions; therefore, it increased the visibility and the film interference color could be observed easily. However, specular reflection only endows humans with seeing objects from a specific single direction. Consequently, when the surface became flat, the film interference color could be hardly observed by maintaining the same observation angle. As a result, an obvious color switching caused by the transformation between wrinkled and flat surfaces was achieved under external strain, such as stretching or bending, demonstrating the interactively visualized strain measurement. Moreover, this color switching was quite sensitive to strain. When a strain of 1.5% was applied, the bright structural color completely disappeared in a certain range of viewing angle.

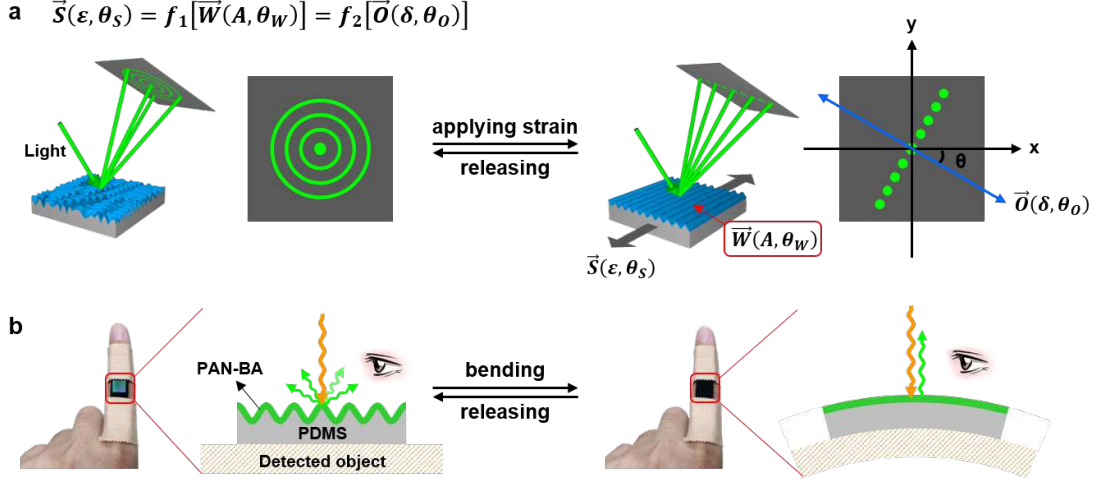


**Fig. 1. Strategy of wearable optical sensor based on surface wrinkles.** **a** Schematic illustration of optical signals changes when accurately detecting the strain utilizing random wrinkles.  $\vec{S}(\varepsilon, \theta_S)$ : strain (magnitude and direction);  $\vec{W}(A, \theta_W)$ : wrinkle (amplitude and direction);  $\vec{O}(\delta, \theta_O)$ : optical signal (viewable angle and orientation of viewable field). **b** Schematic illustration of visualized strain detection.

### Topography evolution of wrinkles under external strain

To gain detailed insight into the working principle of wrinkle-based wearable optical sensors, we first investigated the topography evolution of wrinkles under external strain. According to **Supplementary Equation 6**, the wavelength ( $\lambda$ ) remains almost unchanged at low deformation (strain  $< 10\%$ )<sup>38</sup>, while the amplitude ( $A$ ) is described by **Supplementary Equation 11**. In fact, the  $A$  of the ordered wrinkles decreases indeed with the application of parallel strain, as evident in **Figs. 2a and 2c**. The wrinkles were almost eliminated at a strain of  $\sim 2\%$  and could return to the initial state (**Supplementary Fig. 3a**). However, if the applied strain ( $\varepsilon_{\text{applied}}$ ) exceeded a critical value, which was determined by the prestrain ( $\varepsilon_{\text{pre}}$ ), the wrinkles could not return to the original topography and would obtain a higher  $A$  after releasing the applied strain, owing to the change in  $\varepsilon_{\text{pre}}$  when a larger strain was applied. The variation tendency of  $A$  agrees with that of **Supplementary Equation 11**. However, there were some deviations in the details of the variation curve between the experimental results and **Supplementary Equation 11**. As shown in **Fig. 2c**, the decreasing rate slows down with the applied strain, which is not consistent with the calculated result that the decreasing rate should increase. To further verify the results, we conducted the same experiments on the

prestretching-induced wrinkles (**Supplementary Fig. 4**). The same results were observed:  $A$  decreased as a function of applied strain, and the decreasing rate slowed down with the applied strain. Furthermore, the  $A$  of prestretching-induced wrinkles during the prestrain increase was studied (**Supplementary Fig. 5**). At the first compressive processing, the relationship between  $A$  and the prestrain agreed well with Supplementary Equation 11. At the second or subsequent compressive processing, the rate of increase at 0–2% became obviously slower, similar to Fig. 2c and Supplementary Fig. 4b. These results may be ascribed to the plastic deformation of PDMS, which resulted in a deviation between the practical PDMS and the ideal elastic substrate.

Plastic deformation on the PDMS surface was observed after separating the top film (**Supplementary Fig. 6**), and the amplitude of the PDMS surface was  $\sim 100$  nm, which is much lower than that of the bilayer system. Nevertheless, the topography of the PDMS was robust. It remained in the initial state, even under stretching, warping, or heating. Based on these results, we introduced a quantity of sinusoidal predeformation into the PDMS substrate (**Supplementary Equation 12**) and calculated a modified  $A$ , as described by **Equation 1**.

$$A = h \sqrt{\frac{\varepsilon_{pre} - \varepsilon_{applied} - \varepsilon_c}{\varepsilon_c} + \frac{2 A_0}{3 A}} \quad (1)$$

Where  $h$  represents the skin layer thickness;  $\varepsilon_c$  refers to the critical strain that triggers wrinkle formation in the traditional equation, and is given by **Supplementary Equation 8**;  $A_0$  represents the amplitude of the sinusoidal predeformation of the PDMS, which is described in **Supplementary Equation 13**. The detailed calculations are shown in **Supplementary Discussion**. Notably, this modified equation described  $A$  well at low deformation, similar to Supplementary Equation 11.

According to the modified equation, the variation tendency of  $A$  shows a correlation with  $A_0$ . With an increase in  $A_0$ , the variation curve of  $A$  becomes increasingly smooth (**Supplementary Fig. 7**). Owing to the practical  $A_0$  of  $\sim 100$  nm, the variation curve type in **Supplementary Fig. 7b** is closest to the experimental values. In fact, the calculated results agree well with the above experiments, considering the example of prestretching-induced wrinkles (**Supplementary Fig. 8**), demonstrating the

applicability of the modified equation. Based on the variation curves, the most sensitive range of strain is 0.5–2% ( $\varepsilon_{\text{pre}}-\varepsilon_{\text{applied}}$ ). Thus, to obtain the best sensitivity, surface wrinkles were prepared with  $\varepsilon_{\text{pre}}$  of  $\sim 2\%$  and the best working range of  $\varepsilon_{\text{applied}}$  was identified as 0–1.5%.

In addition to the ordered wrinkles, the topography evolution of random wrinkles under external strain was also investigated. As shown in **Fig. 2b**, when uniaxial strain is applied, random wrinkles gradually evolve into ordered wrinkles perpendicular to the strain direction. After releasing the applied strain, the wrinkles can return to the initial state or change to ordered wrinkles in another direction, depending on the degree of applied strain (**Supplementary Fig. 3b**). To gain insight into the mechanism, the topography evolution of various oriented wrinkles has been investigated. The  $A$  of the ordered wrinkles increased with the strain applied in the perpendicular direction (**Supplementary Fig. 9**). This result was ascribed to the Poisson effect, in which the film compressed in the parallel direction when stretching in the perpendicular direction. Similarly, the applied strain shows a critical value below which the wrinkles could return to the initial topography (**Supplementary Fig. 10**). In addition, ordered wrinkles under applied strain in the  $30^\circ$  direction exhibited a decreasing  $A$ , similar to but slower than that under strain in the parallel direction (**Supplementary Fig. 11**). Ordered wrinkles under applied strain in the  $60^\circ$  direction exhibited a decrease in  $A$  as well as an evolution of the wrinkled orientation (**Supplementary Fig. 12**). As a result, random wrinkles can be regarded as a group of ordered wrinkles in various directions, and thus could evolve into orientated wrinkles under external strain owing to the same mechanism. Furthermore, we defined the average orientation angle ( $\bar{\varphi}$ ) as given in **Supplementary Equation 23** to describe the average orientation of the wrinkles. As shown in **Fig. 2d**,  $\bar{\varphi}$  of random wrinkles decreases as a function of applied strain, indicating that the orientation of wrinkles improves under external strain. In other words, random wrinkles become ordered, and the orientation is perpendicular to the strain direction. These topography evolution results provide a foundation for tuning optical signals by strain-ultrasensitive surface wrinkles.

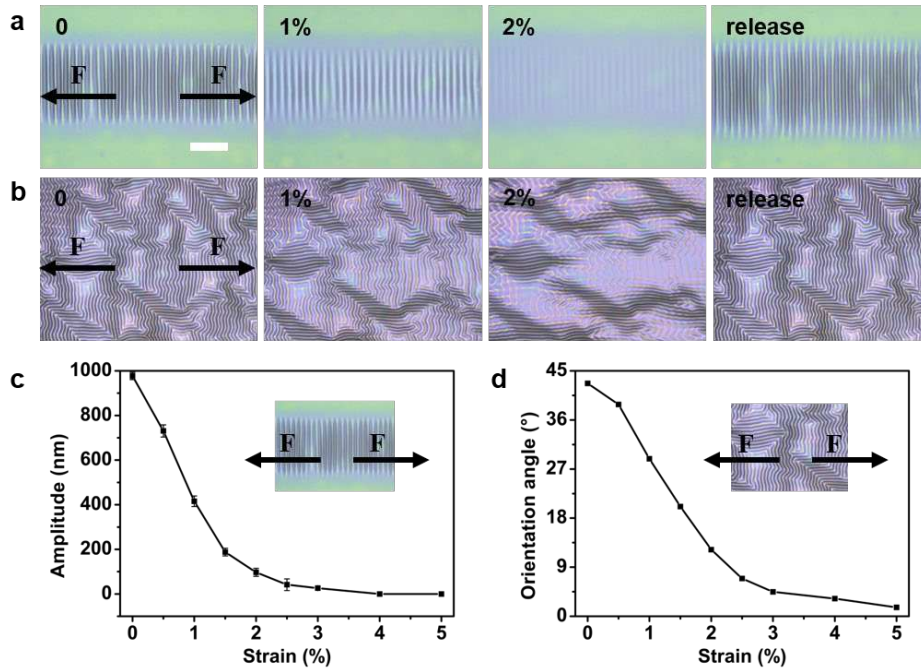


**Fig. 2. Topography evolution of wrinkles under external strain.** **a** Laser scanning confocal microscope (LSCM) images of ordered wrinkles under applied strain in the parallel direction. **b** LSCM images of random wrinkles under applied strain. Scale bar: 100  $\mu\text{m}$ . **c** Amplitude ( $A$ ) of ordered wrinkles as a function of applied strain in the parallel direction. Error bars represent the standard deviations of three independent data. **d** Average orientation angle ( $\bar{\varphi}$ ) of random wrinkles as a function of applied strain.

In addition, the topography evolution of wrinkles under equiaxed strain was investigated (**Supplementary Fig. 13**). The ordered wrinkles gradually disappear with decreasing  $A$  (**Supplementary Figs. 13a and 13b**), similar with Fig. 2a. However, the rate of decrease is much faster than that under uniaxial strain. Under uniaxial strain, the film underwent stretching and compression in orthogonal directions, while under equiaxed strain, the film undergoes stretching in all directions, which results in a more significant effect than that in a single direction. Moreover, the topography completely returns to the initial state because the applied strain is smaller than  $\epsilon_{\text{pre}}$ . Similarly, random wrinkles also gradually disappear with decreasing  $A$  under equiaxed strain (**Supplementary Figs. 13c and 13d**), which is quite different from those under uniaxial strain, which can also be ascribed to the stretching in all directions.

In addition to stretching, bending is a typical mode of external strain (**Supplementary Fig. 14**). In fact, the bending mode is more common in daily life, such

as finger bending. Thus, we further investigated the topography evolution of wrinkles during bending. Based on the calculations in **Supplementary Discussion**, it can be concluded that the applied strain is linearly correlated with the curvature. Thus, the  $A$  of the ordered wrinkles decreases as a function of curvature in the parallel direction (**Supplementary Figs. 15a and 15c**), similar to that in Figs. 2a and 2c. Similarly, random wrinkles evolve into orientated wrinkles during bending (**Supplementary Figs. 15b and 15d**). Furthermore, either ordered or random wrinkles show reversibility in a certain range determined by  $\varepsilon_{\text{pre}}$  (**Supplementary Fig. 16**), which is the same as the stretching mode. The topography evolution of wrinkles during bending will undoubtedly expand the applications of wrinkle-based wearable sensors.

### Optical signals corresponding to wrinkled topography

Based on the wrinkled topography evolution, we further investigated the change in the reflected optical signals during strain application. First, the static relationship between optical signals and wrinkled topography has been determined. According to the geometry of light propagation, the viewable angle ( $\delta$ ), which is the range where one could see an object, equal to half of the included angle of reflected light ( $2\delta$ ), is determined by the wrinkled topography, as calculated by **Equation 2** (For detailed calculations, see **Supplementary Fig. 17** and **Supplementary Discussion**).

$$2\delta = \sin^{-1} \left[ \frac{\sqrt{1 - \sin^2 \alpha \sin^2 \beta}}{\sqrt{1 + \tan^2 \alpha \cos^2 \beta}} (\sin \gamma_{\max} + \cos \gamma_{\max} \tan \alpha \cos \beta) \right] + \sin^{-1} \left[ \frac{\sqrt{1 - \sin^2 \alpha \sin^2 \beta}}{\sqrt{1 + \tan^2 \alpha \cos^2 \beta}} (\sin \gamma_{\max} - \cos \gamma_{\max} \tan \alpha \cos \beta) \right] \quad (2)$$

Where,  $\alpha$  and  $\beta$  refer to the included angle between the incident light and the normal direction of the surface, and that between the projection of incident light on the surface and the direction of the wrinkle, respectively.  $\gamma$  is the inclination angle of the wrinkle profile, which is described in **Supplementary Equations 26 and 27**.

In other words, when the amplitude of the wrinkle in a certain direction increases, the viewable angle increases correspondingly in the same direction. Conversely, the viewable angle accurately reflects the wrinkle amplitude in a certain direction. On the other hand, the viewable angle can also be measured experimentally using the reflected

diffraction pattern (**Supplementary Equation 33**). Thus, by measuring the image of the diffraction pattern and subsequently calculating the viewable angle, one can easily obtain the information of the wrinkled topography. Importantly, the magnitude of the viewable angle ( $\delta$ ) is correlated with the wrinkle amplitude, and the orientation of the viewable field ( $\theta_o$ ) reflects that of the wrinkle. Thus, it can be concluded that the changes in the reflected optical angles can reflect the evolution of the wrinkled topography in a dynamic process.

Owing to the established relationships between the applied strain, wrinkled topography evolution, and changes in the reflected optical angles, the strain information could be obtained from the viewable field. During strain application, the change in the reflected optical signals imitates the wrinkled topography evolution and further reveals the information of the applied strain. A series of experiments were conducted to investigate the change in the reflected optical signals during strain application utilizing the diffraction pattern. The measurements were performed in reflection mode using a green laser beam ( $\lambda_{\text{light}} = 532 \text{ nm}$ ) with an incident angle ( $\alpha$ ) of  $30^\circ$ . The screen was perpendicular to the specular reflected light, and the distance between the sample and screen ( $d$ ) was 0.5 m. As shown in **Figs. 3a and 3b**, when external strain is applied, the concentric rings evolve into ellipses and finally into a line, which agrees well with the wrinkled topography evolution from random to orientated wrinkles during strain application. Moreover, the orientation of the diffraction pattern is in accordance with that of the strain. The short axis is parallel to the strain direction, while the long axis is perpendicular to it. As evident in **Fig. 3a**, when the external strain is applied parallel to the x-axis (Here, the projection direction of incident light on the surface has been defined as the x-axis, and the normal direction as the y-axis), the short axis is parallel to the x-axis and its length decreases as a function of applied strain; simultaneously, the long axis is parallel to the y-axis and its length increases as a function of applied strain. However, if the external strain is applied in the  $30^\circ$  direction, the short axis is also in the  $30^\circ$  direction and the long axis is in the  $-60^\circ$  direction (**Fig. 3b**), demonstrating the orientation dependence of optical signals on the strain direction. The length changes exhibit similar results to those shown in Fig. 3a. The detailed viewable angle changes

have been calculated and are summarized in **Figs. 3c and 3d**. Therefore, both the viewable angle in the direction parallel to the applied strain ( $\delta_{\parallel}$  in Fig. 3c and  $\delta_{30^\circ}$  in Fig. 3d) and perpendicular to the applied strain ( $\delta_{\perp}$  in Fig. 3c and  $\delta_{-60^\circ}$  in Fig. 3d) can provide information on the strain magnitude, regardless of the strain direction. The sensor depicts sensitivities  $((\Delta\delta/\delta_0)/\varepsilon$  was defined as the gauge factor to measure the sensitivity) of -44 and 11 in the strain range of 0–1.5% in the parallel and perpendicular directions, respectively. The experimental results agree well with the calculations in **Supplementary Discussion**, demonstrating the feasibility of detecting the strain direction as well as its magnitude using a single optical signal.

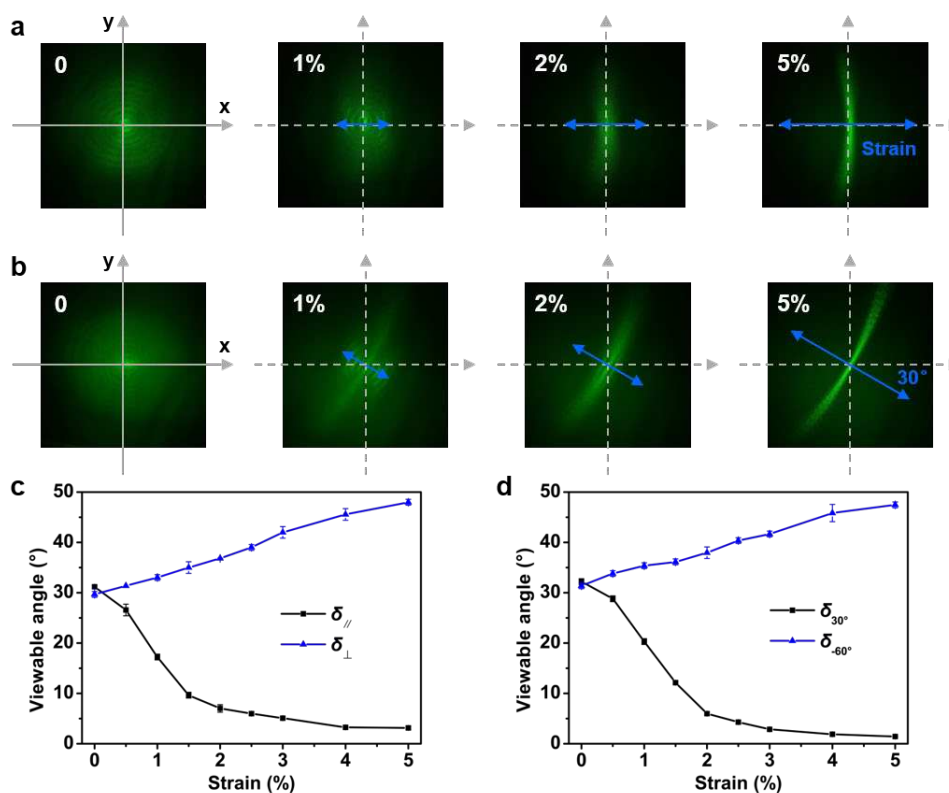


**Fig. 3. Changes in optical signals under external strain for strain direction and magnitude detection.** **a–b** Images of reflected diffraction pattern evolution corresponding to random wrinkles under strain in (a) the parallel direction and (b) the 30° direction. **c–d** Viewable angles corresponding to random wrinkles as a function of strain in (c) the parallel direction and (d) the 30° direction. Error bars represent the standard deviations of three independent data.

Next, we investigated the changes in the reflected optical signals corresponding to ordered wrinkles under strain in different directions. As shown in **Fig. 4a**, when external

strain is applied in the parallel direction, the diffraction pattern evolves from that of a lattice to a spot, which agrees well with the wrinkled topography evolution shown in Fig. 2a, where ordered wrinkles gradually became flat. Correspondingly,  $\delta_{//}$  decreases as a function of the applied strain, while  $\delta_{\perp}$  remains almost unchanged. Therefore,  $\delta_{//}$  accurately reflects strain magnitude. Moreover, the change in  $\delta_{//}$  corresponding to the ordered wrinkles (Fig. 4a) is almost the same as that corresponding to random wrinkles (Fig. 3c), which may be ascribed to the wrinkle amplitude in the parallel direction exhibiting the same decreasing tendency in ordered wrinkles and random wrinkles, independent of wrinkle amplitude in other directions. Thus, viewable angles corresponding to ordered wrinkles could also be used to detect the strain magnitude when fixing the strain direction parallel to the surface wrinkles. In addition, the changes in the reflected optical signals corresponding to the ordered wrinkles under strain in other directions have also been investigated. Under applied strain in the perpendicular direction, the diffraction pattern corresponding to the ordered wrinkles become longer (**Supplementary Fig. 18**), because of the increasing amplitude shown in Supplementary Fig. 9. Under applied strain in the 30° direction, the diffraction pattern becomes shorter, similar to but slower than that under strain in the parallel direction (**Supplementary Fig. 19**). Under applied strain in the 60° direction, the diffraction pattern exhibits not only a decreasing length, but also a morphological evolution (**Supplementary Fig. 20**), which agrees well with the wrinkled topography in Supplementary Fig. 12. The corresponding viewable angle changes are summarized in **Supplementary Fig. 21**. These results provide proof of the evolution of optical signals corresponding to random wrinkles. Thus, the diffraction pattern corresponding to the random wrinkles evolved from concentric rings into ellipses and finally into a line.

Furthermore, the reversibility and stability of wrinkle-based optical sensors have been investigated. Taking ordered wrinkles as an example, when an external strain was applied in the parallel direction, the viewable angles were highly repeatable under cyclic strains. As shown in **Fig. 4b**,  $\delta_{//}$  under different strains ranging from 0.5% to 2% almost completely recovers to the initial values after releasing the strain, demonstrating excellent strain-sensing reversibility in the working range. The wrinkle-based optical

sensor works stably for at least 500 stretching/releasing cycles under 2% strain (**Fig. 4c**). Moreover, the loading-unloading curves at the 1<sup>st</sup>, 50<sup>th</sup>, and 500<sup>th</sup> cycles are almost the same, indicating that the hysteresis was almost unchanged after 500 cycles, indicating excellent stability. The response time is governed by the strong adhesion between the film and the substrate, the appropriate elastic nature of PDMS, and the ultrafast propagation of light.

In addition to simultaneously detecting the strain direction and magnitude, we also achieved visualized strain measurements utilizing ordered surface wrinkles. As described above, the viewable angle refers to the range where an object can be seen. Thus, a large viewable angle means that one can easily observe the film interference color, while a small viewable angle limits the visibility of the object. As shown in **Fig. 4a**, when an external strain is applied parallel to the wrinkle orientation,  $\delta_{//}$  decreases rapidly, which indicates that the object becomes increasingly difficult to be seen by human eyes. To further demonstrate the feasibility, the macrographs of an ordered wrinkled surface were in situ recorded during stretching in the parallel direction. As shown in **Fig. 4d**, the bright interference color gradually becomes invisible as the wrinkle amplitude decreases during stretching. Therefore, the strain information can be visualized through the images of the interference color. Moreover, the images completely return to the initial state on releasing the external strain. Significantly, the wrinkle-based visualized sensor exhibits a high sensitivity of ~1.5%, demonstrating the high performance of the sensor in interactively visualizing small strain.

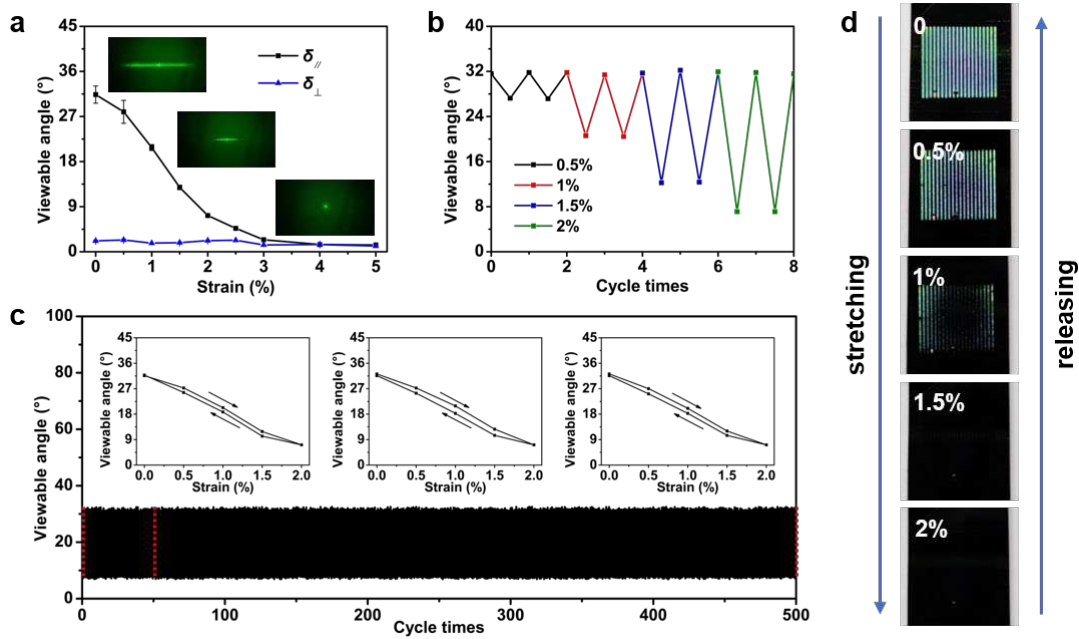


**Fig. 4. Performance of the wearable optical sensor and its visualized strain detection.** **a** Viewable angle and reflected diffraction pattern evolution corresponding to ordered wrinkles under strain in the parallel direction. Error bars represent the standard deviations of three independent data. **b** Changes in viewable angle corresponding to ordered wrinkles under a strain of 0.5%, 1%, 1.5%, and 2% in the parallel direction. **c** The reversible changes in viewable angle corresponding to ordered wrinkles under 500 cycles of 2% strain. Insets show the detailed data at 1<sup>st</sup>, 50<sup>th</sup>, and 500<sup>th</sup> cycles, respectively. **d** Macrographs of ordered wrinkled surface under stretching/releasing cycle in the parallel direction.

### Applications of wearable optical sensors

To demonstrate the potential applications of wearable optical sensors based on surface wrinkles in detecting complex slight strain, we conducted a series of experiments on the human body and many other objects. First, an ordered wrinkle-based sensor was applied to the human wrist and prosthetic wrist. As shown in **Figs. 5a and 5b**, when the human wrist or prosthetic wrist is slightly bent to a small degree, the bright interference color of a sensor attached to the joint quickly becomes invisible, demonstrating the visualized detection of subtle strain. Notably, the bending degree is so small that it can be often neglected by the naked eye, but the sensor successfully amplified the signal because the change in the interference color is conspicuous and can be easily captured by humans. **Supplementary Movie 1** shows the in-situ observation

of the color change of an ordered wrinkle-based sensor attached to the joint during slight bending of the human wrist. In addition to visualized detection, the reflected optical signals provide an accurate detection of the strain simultaneously. As shown in **Fig. 5c**,  $\delta_{//}$  decreases quickly from  $32.6^\circ$  to  $7.7^\circ$  when the prosthetic wrist is bent by  $2^\circ$ . Therefore, an accurate wrist bending degree could be obtained through the reflected diffraction pattern and the corresponding viewable angle. Similarly, a random wrinkle-based sensor also provided an accurate detection of the strain. With prosthetic wrist bending,  $\delta_{//}$  decreased, and  $\delta_{\perp}$  increased. Thus, the bending degree can be identified from either of them. **Supplementary Movie 2** shows the in-situ observation of the reflected diffraction pattern evolution corresponding to ordered wrinkles and random wrinkles attached to the joint during slight bending of the human wrist. In addition to the wrist, a wearable optical sensor has also been applied to other places, such as a human finger and a prosthetic finger. In all the cases, the sensor displayed similar results to that on a wrist (**Fig. 1b and Supplementary Fig. 22, Supplementary Movie 3**), demonstrating the reliability and versatility of the wearable optical sensor.

The wrinkle-based optical sensor can not only detect uniaxial strain, but also multiaxial motion. Considering a random wrinkle-based sensor attached to the joint of a prosthetic wrist as an example, the optical signals were observed to change as shown in Fig. 5c during wrist bending, while it was quite different when the wrist rotated (**Fig. 5d**). In the initial state, random wrinkles displayed a bright structural color on the whole surface, with a corresponding viewable angle of  $\sim 32^\circ$  in all directions. When the wrist rotated to the right, half of the surface wrinkles underwent stretching while the other half underwent compression. As a result, random wrinkles evolved into ordered wrinkles, the directions of which were orthogonal in different regions. Therefore, only half of the surface structural color could be observed in a specific direction, while the other half could be observed from the perpendicular direction. Correspondingly, the diffraction patterns evolved into lines, and  $\delta_{\perp}$  corresponding to the right half increased to  $49.5^\circ$ , while  $\delta_{//}$  corresponding to the left half increased to  $44.4^\circ$ . Furthermore, similar but converse results were observed when the wrist rotated to the left. In summary, the optical signal changes are quite different during the different motions.

Therefore, the motion type as well as the motion direction and magnitude can be judged through the reflected optical signals, demonstrating the potential applications of the proposed sensor in detecting complex slight strains.

In addition to the human body, this optical sensor can also be used in many other areas to detect slight strain. As shown in **Fig. 5e**, it has been successfully applied to a bridge model to simulate the visualized detection of bridge deformation. In the initial state, the striped wrinkled surface displays a bright structural color, which can be easily captured by the naked eye. However, after a slight deformation of the bridge, which is hardly visible to a human while looking from the top down, the wrinkled surface becomes flat, leading to the invisibility of the structural color. The conspicuous color change undoubtedly amplifies the signal and provides visualized detection of slight deformation or vibration of the bridge, which demonstrates its versatility and potential applications in various fields.

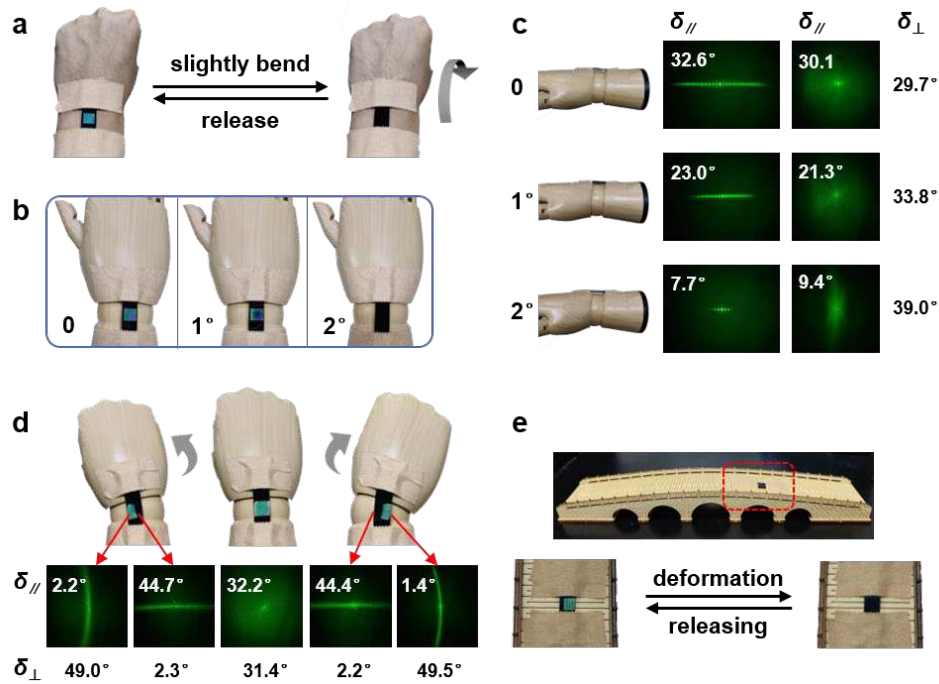


**Fig. 5. Applications of wearable optical sensor based on surface wrinkles. a–b** Photographs of an ordered wrinkle-based sensor detecting (a) a human wrist bending and (b) a prosthetic wrist bending. **c** Viewable angle and reflected diffraction pattern evolution corresponding to ordered wrinkles and random wrinkles during a prosthetic wrist bending. **d** Photographs of a random wrinkle-based sensor detecting a prosthetic wrist rotation and corresponding reflected diffraction pattern. **e** Photographs of an ordered wrinkle-based sensor detecting slight deformation of a bridge model.

## Discussion

In summary, we demonstrate a facile and robust strategy for wearable optical sensors based on surface wrinkles ultrasensitive to strain. Owing to the vector property of the optical signal, the strain magnitude and direction can be detected simultaneously using a single optical signal. Thus, the motion type, direction, and magnitude can be obtained through the changes in reflected optical signals owing to the established correlative function between the strain ( $\vec{S}(\varepsilon, \theta_S)$ ), the wrinkled topography ( $\vec{W}(A, \theta_W)$ ), and the optical signals ( $\vec{O}(\delta, \theta_O)$ ) in the bilayer wrinkling system. By using this wrinkle-based sensor, visual detection of slight strain has also been achieved owing to the conspicuous change in the film interference color. A strain signal less than  $\sim 1.5\%$  was successfully amplified, which was hardly visible to the naked eye. This provides an alternative strategy for wearable optical sensors with convenient strain direction and magnitude detection, interactively visualized measurement, and relatively high sensitivity. In addition, it possesses advantages such as electrical safety and immunity to electromagnetic interference. In future works, the strategy can be further improved by developing a software, so that the whole information of strain can be easily read out by simply capturing the image of diffraction pattern using a mobile phone. It is believed that the proposed strategy may find potential applications in detecting complex slight strains, such as subtle human motion or deformation of an object.

## Methods

### Preparation of PDMS substrate

The PDMS elastic sheet was prepared by mixing PDMS prepolymer (Sylgard 184, Dow Corning) in a 10:1 base/curing agent ratio, followed by drop-coating in a Petri dish, degassing in a vacuum oven, and curing at 70 °C for 4 h (thickness approximately 400  $\mu\text{m}$ ). Then the sample was cut into 1 cm  $\times$  1 cm squares and 1 cm  $\times$  5 cm rectangles.

### Preparation of CNT-PDMS substrate

PDMS base agent (15 g) and multiwalled carbon nanotubes (15 mg, 0.1 wt%) were mixed in 20 ml toluene and subjected to ultrasonic treatment for 12 h. Then the mixture was dried in an oven at 70 °C for 10 h to remove the solvent. The obtained CNT-containing PDMS base was mixed with 1.5 g curing agent (base/curing agent ratio was 10:1). The mixture was poured into a Petri dish, degassed in a vacuum oven, and cured at 70 °C for 4 h (thickness approximately 400 µm). Then the sample was cut into 1 cm × 1 cm squares and 1 cm × 5 cm rectangles.

### **Preparation of surface wrinkle pattern**

As for thermal treatment induced wrinkles, a toluene solution of PAN-BA (6 wt%) was spin-coated onto a PDMS sheet to prepare the skin layer. The bilayer samples were irradiated with/without photomask by 365 nm UV light for 15 min and heated at 85 °C. When cooling to room temperature, ordered/random wrinkled patterns occurred. Then the samples were cured on a vernier caliper.

As for prestretching induced wrinkles, a toluene solution of PAN-BA (6 wt%) was spin-coated onto a PDMS sheet to prepare the skin layer. The samples were cured on a vernier caliper and prestretched for 10%. After irradiated by 365 nm UV light for 15 min, 2% or 6% prestrain was released and ordered wrinkled patterns occurred.

### **Stretching of surface wrinkle pattern**

As for uniaxial stretching, the samples were cured on a vernier caliper and stretched. The applied strain was measured by the vernier caliper. As for equiaxed stretching, the samples underwent thermal treatment. The applied strain was calculated by coefficient of thermal expansion and temperature variation.

### **Data availability**

The data supporting the findings of this study are available within the paper and its Supplementary Information files.

### **References**

1. Amjadi M., Kyung K.-U., Park I. & Sitti M. Stretchable, Skin-Mountable, and Wearable Strain Sensors and Their Potential Applications: A Review. *Adv. Funct. Mater.* **26**, 1678-1698 (2016).
2. Yang J. C., Mun J., Kwon S. Y., Park S., Bao Z. & Park S. Electronic Skin: Recent Progress and Future Prospects for Skin-Attachable Devices for Health Monitoring, Robotics, and Prosthetics. *Adv. Mater.* **31**, e1904765 (2019).
3. Kang D., et al. Ultrasensitive mechanical crack-based sensor inspired by the spider sensory system. *Nature* **516**, 222-226 (2014).
4. Ling Y., An T., Yap L. W., Zhu B., Gong S. & Cheng W. Disruptive, Soft, Wearable Sensors. *Adv. Mater.* **32**, e1904664 (2020).
5. Trung T. Q. & Lee N. E. Flexible and Stretchable Physical Sensor Integrated Platforms for Wearable Human-Activity Monitoring and Personal Healthcare. *Adv. Mater.* **28**, 4338-4372 (2016).
6. Wang C., et al. Carbonized Silk Fabric for Ultrastretchable, Highly Sensitive, and Wearable Strain Sensors. *Adv. Mater.* **28**, 6640-6648 (2016).
7. Xu K., et al. A Wearable Body Condition Sensor System with Wireless Feedback Alarm Functions. *Adv. Mater.* **33**, e2008701 (2021).
8. Yamada T., et al. A stretchable carbon nanotube strain sensor for human-motion detection. *Nat. Nanotechnol* **6**, 296-301 (2011).
9. Chou H. H., et al. A chameleon-inspired stretchable electronic skin with interactive colour changing controlled by tactile sensing. *Nat. Commun.* **6**, 8011 (2015).
10. Sekitani T. & Someya T. Stretchable organic integrated circuits for large-area electronic skin surfaces. *MRS Bull.* **37**, 236-245 (2012).
11. Tang L., Shang J. & Jiang X. Multilayered electronic transfer tattoo that can enable the crease amplification effect. *Sci. Adv.* **7**, eabe3778 (2021).
12. Kim J., et al. Stretchable silicon nanoribbon electronics for skin prosthesis. *Nat. Commun.* **5**, 5747 (2014).
13. Gu G., et al. A soft neuroprosthetic hand providing simultaneous myoelectric control and tactile feedback. *Nat. Biomed. Eng.*, (2021). Doi: 10.1038/s41551-021-00767-0.
14. Qi D., Zhang K., Tian G., Jiang B. & Huang Y. Stretchable Electronics Based on PDMS Substrates. *Adv. Mater.* **33**, e2003155 (2021).
15. Wang C., Xia K., Wang H., Liang X., Yin Z. & Zhang Y. Advanced Carbon for Flexible and Wearable Electronics. *Adv. Mater.* **31**, e1801072 (2019).
16. Wang X., Dong L., Zhang H., Yu R., Pan C. & Wang Z. L. Recent Progress in Electronic Skin. *Adv Sci (Weinh)* **2**, 1500169 (2015).
17. Ho D. H., Sun Q., Kim S. Y., Han J. T., Kim D. H. & Cho J. H. Stretchable and Multimodal All Graphene Electronic Skin. *Adv. Mater.* **28**, 2601-2608 (2016).
18. Li T., Wang Y., Li S., Liu X. & Sun J. Mechanically Robust, Elastic, and Healable Ionogels for Highly Sensitive Ultra-Durable Ionic Skins. *Adv. Mater.* **32**, e2002706 (2020).
19. Wen J., et al. Multifunctional Ionic Skin with Sensing, UV-Filtering, Water-Retaining, and Anti-Freezing Capabilities. *Adv. Funct. Mater.* **31**, 2011176 (2021).
20. Yan W., et al. Giant gauge factor of Van der Waals material based strain sensors. *Nat. Commun.* **12**, 2018 (2021).
21. Yang T., et al. Hierarchically Microstructure-Bioinspired Flexible Piezoresistive Bioelectronics. *ACS Nano* **15**, 11555-11563 (2021).

22. Bae G. Y., et al. Linearly and Highly Pressure-Sensitive Electronic Skin Based on a Bioinspired Hierarchical Structural Array. *Adv. Mater.* **28**, 5300-5306 (2016).
23. Cai Y., et al. Extraordinarily Stretchable All-Carbon Collaborative Nanoarchitectures for Epidermal Sensors. *Adv. Mater.* **29**, 1606411 (2017).
24. Feng B., et al. Nacre-Inspired, Liquid Metal-Based Ultrasensitive Electronic Skin by Spatially Regulated Cracking Strategy. *Adv. Funct. Mater.* **31**, 1606411 (2021).
25. Xue F., et al. An ultra-broad-range pressure sensor based on a gradient stiffness design. *Mater. Horiz.* **8**, 2260-2272 (2021).
26. Ji B., Zhou Q., Hu B., Zhong J., Zhou J. & Zhou B. Bio-Inspired Hybrid Dielectric for Capacitive and Triboelectric Tactile Sensors with High Sensitivity and Ultrawide Linearity Range. *Adv. Mater.* **33**, e2100859 (2021).
27. Mannsfeld S. C., et al. Highly sensitive flexible pressure sensors with microstructured rubber dielectric layers. *Nat Mater* **9**, 859-864 (2010).
28. Yun S., et al. Polymer-waveguide-based flexible tactile sensor array for dynamic response. *Adv. Mater.* **26**, 4474-4480 (2014).
29. Koeppel R., Bartu P., Bauer S. & Sariciftci N. S. Light- and Touch-Point Localization using Flexible Large Area Organic Photodiodes and Elastomer Waveguides. *Adv. Mater.* **21**, 3510-3514 (2009).
30. Jinno H., et al. Self-powered ultraflexible photonic skin for continuous bio-signal detection via air-operation-stable polymer light-emitting diodes. *Nat. Commun.* **12**, 2234 (2021).
31. Wang C., et al. User-interactive electronic skin for instantaneous pressure visualization. *Nat Mater* **12**, 899-904 (2013).
32. Yokota T., et al. Ultraflexible organic photonic skin. *Sci. Adv.* **2**, e1501856 (2016).
33. Wang Y., et al. Interactively Full-Color Changeable Electronic Fiber Sensor with High Stretchability and Rapid Response. *Adv. Funct. Mater.* **30**, 2000356 (2020).
34. Zhao K., et al. Interactively mechanochromic electronic textile sensor with rapid and durable electrical/optical response for visualized stretchable electronics. *Chem. Eng. J.* **426**, 130870 (2021).
35. Hellebrekers T., Kroemer O. & Majidi C. Soft Magnetic Skin for Continuous Deformation Sensing. *Adv. Intell. Syst.* **1**, 1900025 (2019).
36. Khang D. Y., Jiang H., Huang Y. & Rogers J. A. A stretchable form of single-crystal silicon for high-performance electronics on rubber substrates. *Science* **311**, 208-212 (2006).
37. Bowden N., Brittain S., Evans A. G., Hutchinson J. W. & Whitesides G. M. Spontaneous formation of ordered structures in thin films of metals supported on an elastomeric polymer. *Nature* **393**, 146-149 (1998).
38. Chung J. Y., Nolte A. J. & Stafford C. M. Surface wrinkling: a versatile platform for measuring thin-film properties. *Adv. Mater.* **23**, 349-368 (2011).
39. Hou H., Yin J. & Jiang X. Smart Patterned Surface with Dynamic Wrinkles. *Acc. Chem. Res.* **52**, 1025-1035 (2019).
40. Xu C., Stiubianu G. T. & Gorodetsky A. A. Adaptive infrared-reflecting systems inspired by cephalopods. *Science* **359**, 1495-1500 (2018).
41. Xu C., Colorado Escobar M. & Gorodetsky A. A. Stretchable Cephalopod-Inspired Multimodal Camouflage Systems. *Adv. Mater.* **32**, 1905717 (2020).
42. Wang Y., et al. Controlling silk fibroin conformation for dynamic, responsive, multifunctional,

- micropatterned surfaces. *Proc. Natl. Acad. Sci. U. S. A.* **116**, 21361-21368 (2019).
43. Zong C., et al. Tuning and Erasing Surface Wrinkles by Reversible Visible-Light-Induced Photoisomerization. *Angew. Chem. Int. Ed.* **55**, 3931-3935 (2016).
  44. Li F., Hou H., Yin J. & Jiang X. Near-infrared light-responsive dynamic wrinkle patterns. *Sci. Adv.* **4**, eaar5762 (2018).
  45. Zhou L., Hu K., Zhang W., Meng G., Yin J. & Jiang X. Regulating surface wrinkles using light. *Natl. Sci. Rev.* **7**, 1247-1257 (2020).
  46. Zhang H., et al. Anisotropic, Wrinkled, and Crack-Bridging Structure for Ultrasensitive, Highly Selective Multidirectional Strain Sensors. *Nano-Micro Lett.* **13**, 122 (2021).
  47. Zhang F., et al. Anisotropic conductive networks for multidimensional sensing. *Mater. Horiz.* **8**, 2615-2653 (2021).
  48. Kim K. K., et al. Highly Sensitive and Stretchable Multidimensional Strain Sensor with Prestrained Anisotropic Metal Nanowire Percolation Networks. *Nano Lett.* **15**, 5240-5247 (2015).
  49. Larson C., et al. Highly stretchable electroluminescent skin for optical signaling and tactile sensing. *Science* **351**, 1071-1074 (2016).
  50. Wang X., et al. Full Dynamic-Range Pressure Sensor Matrix Based on Optical and Electrical Dual-Mode Sensing. *Adv. Mater.* **29**, 1605817 (2017).
  51. Hou H., Li F., Su Z., Yin J. & Jiang X. Light-reversible hierarchical patterns by dynamic photo-dimerization induced wrinkles. *J. Mater. Chem. C* **5**, 8765-8773 (2017).

## Acknowledgements

The authors thank National Nature Science Foundation of China (52025032 and 52103144) for their financial support.

## Author Contributions

X. J. and J. Y. conceived the research and analyzed the results and data; T. M. carried out the material synthesis and characterization; S. C. and J. L. took part in some work of material synthesis. All authors contributed to the manuscript.

## Competing interests

The authors declare no competing interests.

## Additional information

**Supplementary information** The online version contains supplementary material available at <https://doi.org/10.1038/XXXX>.

**Correspondence** and requests for materials should be addressed to X. J.

## Supplementary Files

This is a list of supplementary files associated with this preprint. Click to download.

- [SupplementaryInformation.docx](#)
- [Supplementarymovie3.mp4](#)
- [Supplementarymovie2.mp4](#)
- [Supplementarymovie1.mp4](#)